

# Multiple shocks generated by the 2024 May 14 coronal mass ejection

Mohamed Nedal (محمد نضال)<sup>1,\*</sup>, Catherine Cuddy<sup>1,2</sup>, David M. Long<sup>2</sup>, Shilpi Bhunia<sup>1,3,4</sup>,  
Pietro Zucca<sup>5</sup>, and Peter T. Gallagher<sup>1</sup>

- <sup>1</sup> Astronomy & Astrophysics Section, School of Cosmic Physics, Dublin Institute for Advanced Studies, DIAS Dunsink Observatory, Dublin D15 XR2R, Ireland  
<sup>2</sup> Centre for Astrophysics & Relativity, School of Physical Sciences, Dublin City University, Glasnevin Campus, Dublin D09 V209, Ireland  
<sup>3</sup> School of Physics, Trinity College Dublin, College Green, Dublin 2, Ireland  
<sup>4</sup> LIRA, Observatoire de Paris, PSL Research University, CNRS, Sorbonne Université, Université, Paris Cité, 5 Place Jules Janssen, 92195 Meudon, France  
<sup>5</sup> ASTRON – Netherlands Institute for Radio Astronomy, Oude Hoogeveensedijk 4, 7991 PD Dwingeloo, The Netherlands

Received 4 July 2025 / Accepted 13 February 2026

## ABSTRACT

**Context.** A series of powerful solar flares and coronal mass ejections (CMEs) occurred between 10 and 14 May 2024. As these eruptions propagated through the corona, they generated multiple solar type II radio bursts, indicating the presence of shock waves.

**Aims.** This study characterises a series of type II radio bursts associated with a CME that occurred on 14 May, focusing on the coronal conditions during the event and identifying the likely location of the shocks where the radio bursts are generated.

**Methods.** The CME was tracked using a combination of white light and extreme ultraviolet observations of the solar corona taken by three instruments: the Geostationary Operational Environmental Satellite (GOES) Solar Ultraviolet Imager (SUVI) and two coronagraphs of the Solar and Heliospheric Observatory (SOHO) Large Angle and Spectrometric Coronagraph (LASCO), together with ground-based radio observations between 10–240 MHz from the Irish Low-Frequency Array (I-LOFAR). The radial distances of the radio sources were examined using a series of density models, with both potential field source surface and magnetohydrodynamic models used to examine the coronal plasma conditions.

**Results.** Four type II bursts were identified in the I-LOFAR radio dynamic spectrum over ~15 minutes, exhibiting features such as band splitting, herringbones, and fragmentation. The shocks were found to have speeds ranging between ~443–2075 km s<sup>-1</sup>, with drift rates of ~-361 to -78 kHz s<sup>-1</sup>. The shocks were found to have a  $M_A \approx 3.21-3.57$ , indicating that they were super-Alfvénic. The first type II burst was triggered ~18 minutes after the CME launch, with each burst appearing to have been generated at a different height in the corona. Analysis of the derived kinematics and modelling results suggests that the type II bursts were likely produced at the shoulders of the CME near the flanks, where open magnetic field lines and relatively low Alfvén speeds facilitated shock formation.

**Conclusions.** This multi-instrument study shows that multiple type II bursts from a single CME originated at different coronal heights, with modelling indicating their generation near the CME flanks where low Alfvén speeds and open magnetic field lines facilitated shock formation. The findings highlight the role of coronal conditions, particularly the magnetic field configuration and the Alfvén speed distribution, in determining the heights and locations where these bursts originate. Our results reinforce the importance of continuous, multi-wavelength observations for understanding shock dynamics and improving constraints on coronal models.

**Key words.** Sun: activity – Sun: corona – Sun: coronal mass ejections (CMEs) – Sun: flares – Sun: magnetic fields – Sun: radio radiation

## 1. Introduction

Coronal mass ejections (CMEs) are dynamic expulsions of magnetised plasma from the solar corona, commonly observed in coronagraph images as bright, structured features propagating outwards from the Sun. Coronal mass ejection observations consistently reveal a three-part structure: a luminous leading edge, a low-density cavity, and a bright, complex core (Vourlidas 2014; Song et al. 2019, 2023). The leading edge, composed of compressed coronal plasma, indicates the CME's magnetically closed region. The core typically corresponds to an erupting prominence, while the intervening dark cavity is interpreted as a region of reduced density, likely housing a magnetic flux

rope. Understanding their initiation mechanisms and propagation characteristics remains an active area of research.

Coronal shock waves arise from various processes in the Sun's atmosphere and play a significant role in space weather. They are commonly driven by CMEs, flares, and jets (Patsourakos & Vourlidas 2012; Nitta et al. 2013; Zucca et al. 2014; Long et al. 2017; Maguire et al. 2021; Jarry et al. 2023; Nedal et al. 2024) and serve as efficient accelerators of solar energetic particles (Kozarev et al. 2022), often causing disturbances in the heliosphere and Earth's magnetosphere (Liu et al. 2011). Their formation and evolution depend on interactions between the expanding CME, the surrounding plasma, and the solar magnetic field (cf. Long et al. 2019). As a CME propagates outwards, it compresses the ambient plasma, generating shock fronts that can accelerate charged particles

\* Corresponding author: mohamed.nedal@dias.ie

and alter the surrounding plasma and magnetic environment, sometimes triggering additional disturbances (Toida & Uragami 2013; Frassati et al. 2019; Nedal et al. 2025).

These shocks are observable using coronagraph imaging, spectroscopic measurements, and in situ spacecraft data (Vourlidas & Bemporad 2012). Coronal shocks can accelerate particles to high energies, sometimes leading to extreme space weather events (Kilpua et al. 2017). Their interaction with Earth's magnetosphere can induce geomagnetic storms, potentially forming new radiation belts that expose satellites to heightened radiation levels, with some storms reaching intensities comparable to the Carrington event (Tsurutani & Lakhina 2014; Li et al. 2025).

Numerical simulations suggest that expanding cylindrical pistons, such as CMEs, drive magnetosonic waves, leading to the initiation and evolution of large-scale coronal waves (Lulić et al. 2013). Recent advancements in observational techniques and modelling have improved our ability to study shock properties—such as strength, speed, and magnetic field orientation—in the low corona and inner heliosphere (Long et al. 2011; Vourlidas & Bemporad 2012; Nitta et al. 2013; Kozarev et al. 2015, 2022; Nedal et al. 2024). Observing shocks off the solar limb is particularly advantageous for minimising projection effects, which can introduce uncertainties in determining their time-dependent positions and structure (Kozarev et al. 2015).

The evolution of large-amplitude perturbations can result in the formation of magnetohydrodynamic (MHD) shock waves, often quasi-perpendicular (Lulić et al. 2013), though quasi-parallel geometries have also been shown to produce type II radio bursts (Holman & Pesses 1983; Knock & Cairns 2005). The evolution of large-amplitude perturbations can result in the formation of perpendicular MHD shock waves, which are relevant for type II radio bursts.

Coronal shocks play a key role in generating type II bursts by accelerating electrons in the solar corona and interplanetary medium (Mann et al. 2022; Koval et al. 2023; Raja et al. 2023). These shock waves, often associated with CMEs, provide the necessary conditions for plasma emission in the radio spectrum. Type II bursts serve as indicators of shock-driven particle acceleration, offering valuable data for the early detection of solar storm disturbances and space weather implications (Raja et al. 2023). The occurrence of type II bursts has been linked to CME-driven shocks, although they can also arise independently of CMEs (Morosan et al. 2023; Kumari et al. 2023). These bursts exhibit fine structures due to the complex nature of shock waves and their interactions with coronal plasma (Koval et al. 2023). They are characterised by fundamental (F) and harmonic (H) emission bands, corresponding to plasma emission at the local electron plasma frequency and its second harmonic, respectively (Mann et al. 1995). The frequency drift rate of type II bursts reflects the shock wave's motion through the varying plasma density of the corona, providing insight into shock dynamics (Vršnak et al. 2001; Chernov & Fomichev 2021).

Spectral features such as band splitting, herringbone patterns, and spectral breaks serve as valuable diagnostics for understanding shock-corona interactions (Koval et al. 2023). Band splitting has been attributed to emissions from the upstream and downstream regions of the shock front (Zimovets et al. 2012; Chrysaphi et al. 2018) or from multiple parts of the shock (Bhunia et al. 2023; Morosan et al. 2023). Furthermore, previous studies have reported radio observations of multiple lanes of type II bursts, likely originating from distinct regions of the shock front (Zimovets & Sadykov 2015; Lv et al. 2017). Spectral breaks have been associated with abrupt

changes in ambient plasma conditions. For instance, Kong et al. (2012) observed a sudden frequency drop in a type II burst's H component, interpreted as a shock propagating across a streamer boundary with a sharp plasma density decrease. Similarly, Zhang et al. (2024) reported a spectral bump in a type II burst, likely caused by the shock encountering a localised low-density region, such as a coronal hole.

Forward and reverse herringbones, observed in type II bursts, are produced by shock-accelerated electrons propagating along open field lines (Abidin et al. 2023). These structures provide insights into electron acceleration mechanisms. Additionally, type II bursts exhibit various fine structures that can result from the shock encountering turbulent regions with varying density and magnetic field configurations (Magdalenic et al. 2020; Ramesh et al. 2023). Imaging spectroscopy studies indicate that small-scale motions of fine structures are driven by turbulence in different regions of the corona (Bhunia et al. 2023).

Given the importance of understanding these various structures, we conducted a detailed investigation of type II bursts and their associated CMEs. On 2024 May 14, we observed four type II bursts with distinct morphologies using the Irish Low-Frequency Array (I-LOFAR) station in high resolution. The driver CME was tracked using three instruments: the Geostationary Operational Environmental Satellite (GOES) Solar Ultraviolet Imager (SUVI) and the Solar and Heliospheric Observatory (SOHO) Large Angle and Spectrometric Coronagraph (LASCO) C2 and C3. Section 2 describes the instruments, observations, and analysis techniques. Section 3 presents the results. Section 4 presents the interpretation. Finally, in Sect. 5, we summarise our findings.

## 2. Observations and data analysis

On 14 May 2024, a series of nine CMEs were observed by the SOHO-LASCO instrument and catalogued by the Coordinated Data Analysis Workshops (CDAW) catalogue<sup>1</sup>, culminating in two fast halo-CMEs late in the day. We focus on the final CME, which first appeared in the GOES-SUVI 195 Å images at ~17:12 UT and was associated with a well-defined large-scale extreme ultraviolet (EUV) wave. The wavefront was tracked from 1.17 to 1.92  $R_{\odot}$  in SUVI, followed by its continued outward propagation observed by LASCO C2 (2.78–7.08  $R_{\odot}$ ) between ~17:48 and 18:24 UT, and LASCO C3 (4.00–30.55  $R_{\odot}$ ) between ~17:54 and 23:01 UT. This CME originated from AR13680 (N17E72), which also produced an M4.5-class flare that began at 17:25 UT, peaked at 17:28 UT, and ended by ~17:55 UT. Approximately 40 minutes earlier, an unrelated but temporally proximate X8.7-class flare erupted from AR13664 near the western limb (S18W89), peaking at 16:51 UT and concluding at 17:02 UT.

### 2.1. EUV and coronagraph imagery

Figure 1 shows a sequence of running-ratio images capturing the temporal progression of the EUV wave observed at the eastern limb of the Sun. The top row reveals the CME as it begins and develops in SUVI 195 Å. The middle and bottom rows display complementary white-light observations from LASCO C2 and LASCO C3, respectively, illustrating the CME's outward propagation through the inner and outer coronagraph fields of view (FOVs). The running-ratio technique was employed to enhance

<sup>1</sup> SOHO/LASCO CME Catalogue: [https://www.sidc.be/cactus/catalog/LASCO/2\\_5\\_0/qk1/2024/05/CME0104/CME.html](https://www.sidc.be/cactus/catalog/LASCO/2_5_0/qk1/2024/05/CME0104/CME.html)

dynamic features, making the expanding CME front and its interaction with the surrounding coronal environment more prominent by showing the evolution of temperature and density much more clearly and much cleaner (Downs et al. 2012).

To analyse the shock wave associated with the CME, we estimated its kinematics along 13 slits separated by  $2^\circ$  angular intervals, spanning from position angle  $58^\circ$  at the shock's upper edge to  $82^\circ$  at its lower edge within the SUVI FOV. The Sun's centre was taken as the common origin point for all the slits across multiple instruments (Fig. 2). For each slit, the intensity values were sampled and stacked over time to make height-time plots (J-plots). We then extracted height-time profiles from the SUVI and LASCO running-ratio images, using a simple point-and-click methodology to track the EUV wave's apex height above the solar limb (Gallagher et al. 2003). To estimate the error, the measurements were repeated five times to calculate the standard error. The distributions of the CME speed and acceleration along the slits are shown in Fig. 3, while the height-time profiles of the shock wave in SUVI and those deduced from the type II bursts are introduced in Fig. 4.

Since we lack direct imaging of the radio sources, we inferred the likely locations of the radio bursts by applying electron-density models to estimate the radial distances at which these bursts were triggered. We used five density models—Allen's model (Allen 1947), Newkirk's model (Newkirk 1961), Saito's model (Saito et al. 1970), Leblanc's model (Leblanc et al. 1998), and Mann's model (Mann et al. 1999)—to determine which best matched the observations in EUV. As the CME evolved and expanded, the portion intersecting the CME across these slits narrowed, reducing variability in the estimated kinematics across the slits over time.

To quantify the CME's lateral dynamics, we fitted a curved triangular envelope to the widest two points across the CME visible in the running-ratio images in SUVI, LASCO C2, and LASCO C3. This allowed us to extract both the lateral expansion speed and angular width over time within each instrument's FOV. Vertex positions were adjusted only to follow the evolving CME's width, enabling a uniform extraction of the triangle base used to quantify the CME angular width and lateral expansion (Figs. 1 and 2). This combined approach provides insight into the detailed variations of the shock wave's expansion and its changing properties with the angular position.

Figure 3 illustrates histograms of the shock speed (top panels) and acceleration (bottom panels) derived across the 13 slits via Savitzky-Golay fitting applied to the kinematic equation of motion (cf. Byrne et al. 2013) for observations by SUVI, LASCO C2, and LASCO C3. Each panel also provides a statistical summary, including the maximum, minimum, mean, standard deviation, and sample count. The top panels show a clear increase in the mean velocity as the wave propagates outwards through the FOV of SUVI and LASCO. SUVI reveals lower speeds, with values ranging between  $\sim 100$ – $917 \text{ km s}^{-1}$ , while LASCO C2 records significantly higher speeds, spanning  $\sim 761$ – $1742 \text{ km s}^{-1}$ . The standard deviations indicate greater variability in speeds as the shock propagates away from the Sun. The bottom panels reveal a range of positive and negative values, which reflect the complex kinematics of the shock wave as it interacts with the coronal medium. SUVI captures a wider acceleration range between  $\sim -550$ – $714 \text{ m s}^{-2}$ , suggesting significant variability near the wave's origin. This also shows that the wave undergoes an impulsive acceleration in the early phase in the low corona, which is aligned with previous studies (Gallagher et al. 2003; Long et al. 2008; Nitta et al. 2013; Kozarev et al. 2015; Nedal et al. 2024). LASCO C2 shows predominantly deceler-

ating behaviour, while LASCO C3 indicates a narrower distribution, reflecting the shock's eventual stabilisation and dissipation. Together, these histograms provide a detailed statistical overview of the shock wave's evolving kinematic properties across multiple regions of the corona.

## 2.2. Radio dynamic spectra

I–LOFAR is part of the European Research Infrastructure Consortium (ERIC). It has low-band (LBA) and high-band (HBA) antennae, which can be used together to observe the full frequency range of the telescope (van Haarlem et al. 2013). The LBA spans 10–90 MHz. Observing with the LBA is called mode 3. The HBA spans 110–240 MHz. Filters divide this band into two sub-bands, 110–190 MHz (mode 5) and 210–240 MHz (mode 7). On 2024 May 14, I–LOFAR observed the Sun in mode 357 continuously between 10:02 UT and 19:07 UT (Fig. 5). In this study, we focus on the segment of I–LOFAR observations between 17:30 UT and 17:48 UT. This corresponds to solar radio emissions associated with the second CME, which erupted from AR3682 on the north-east limb at 17:30 UT. The radio dynamic spectra for this period reveal four short-lived type II bursts, each with a F and H lane and other interesting fine structures. I–LOFAR's high sensitivity and time resolution enable the detection of fine structures such as herringbones. The data were recorded by the REALtime Transient Acquisition (REALTA) system (Murphy et al. 2021). The cadence of the I–LOFAR data we used is 2 ms. To remove the constant background from the spectrum, background subtraction was performed in each band. The band's mean intensity was subtracted from each intensity value.

To visually identify time and frequency points along each type II burst, we first identified the start and end points. Using the dynamic spectra shown in boxes 1–4 of Fig. 5 for each burst lane, we made ten attempts to accurately click on the first and last points on the burst lane and found. These start and end times and frequencies are shown in Table 1. We then plotted 30 vertical lines that were evenly spaced in time between the start and end times of the burst and attempted to click where the middle of the burst lane intercepted these vertical lines (Fig. A.3). We identified the points ten times and found the mean of 30 burst lane points. These were the inputs when we proceeded to calculate an estimate for the radial velocity of the shock at the location of the type II radio sources. For each burst lane, we used a four-fold Newkirk density model to convert each frequency to a height, then performed a linear regression of these height and time points to calculate the radial velocity.

For completeness, we also compared the shock speeds derived from the frequency–drift rates (Morosan et al. 2019) using

$$v = -\frac{2r^2}{\alpha \ln 10 f_p} \frac{df}{dt},$$

with those obtained from the height-time regression. This expression is derived assuming a Newkirk density profile; here we adopt a four-fold Newkirk model ( $\alpha = 4$ ), consistent with the density scaling used throughout this work. Both approaches adopt the four-fold Newkirk density profile, but the drift-rate method depends explicitly on the local density gradient through  $(dn_e/dr)^{-1}$ , whereas the height-time method averages over multiple frequency-height samples to derive a single kinematic trend.

To estimate the Alfvén Mach number of the shock, we used two independent approaches. First, when band splitting

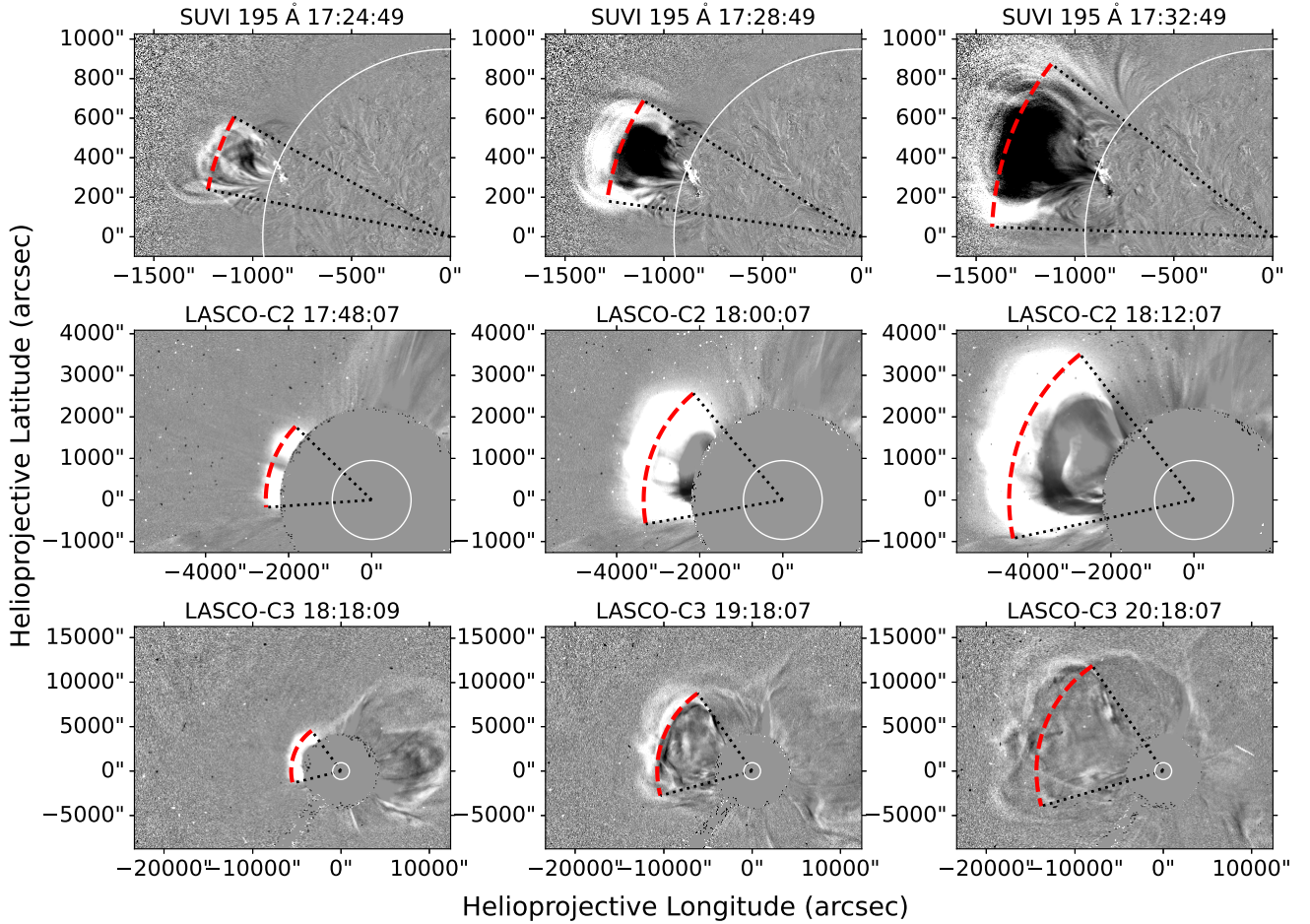


**Fig. 1.** Running-ratio images showing the progression of the CME at the eastern limb from SUVI (top panel), LASCO C2 (middle panel), and LASCO C3 (bottom panel). The arc shape is used to estimate the CME expansion speed and angular width. The black dots represent the upper and lower slits, while the red dashes represent the triangle base, denoting the CME’s width.

was present, we applied the standard density-jump method, deriving the compression ratio from the separation of the split lanes and converting it to a Mach number using the Rankine–Hugoniot relations. This provides a local measurement at the radio-emitting segment of the shock. Second, we estimated a Mach number by dividing the CME leading-edge speed measured along each slit by the local Alfvén speed obtained from the FORWARD model. This approach reflects the large-scale shock kinematics and the model-derived background coronal parameters rather than the immediate plasma at the radio source. See Vršnak et al. (2002), Nedal et al. (2019) for more details on the methods.

### 3. Results

#### 3.1. EUV wave characteristics

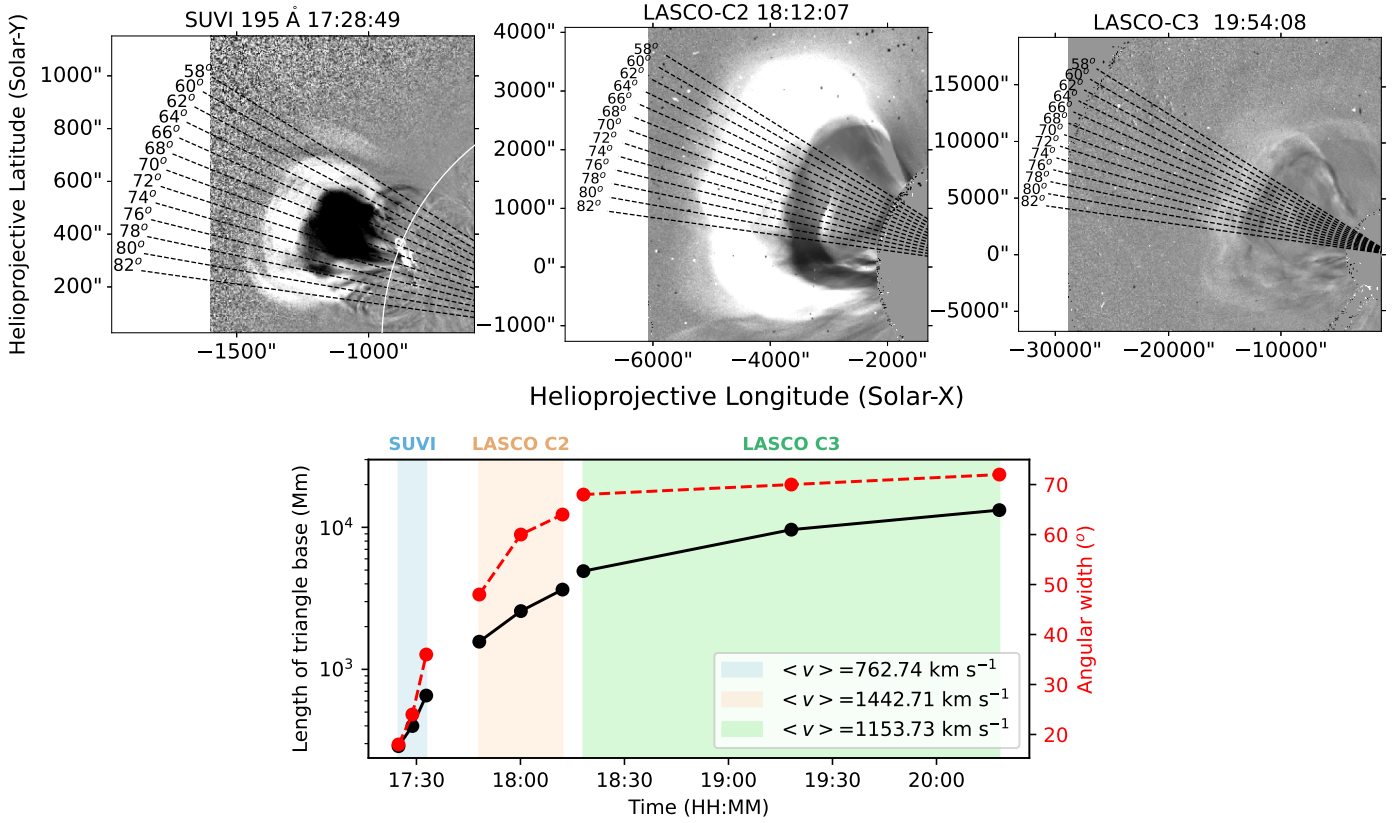
The CME’s expansion was tracked in SUVI, LASCO C2, and LASCO C3 running-ratio images, revealing a continuously broadening front across the eastern limb (Fig. 1). The fitted triangular envelope, defined by the CME’s widest two points, remained geometrically consistent across all frames, enabling a uniform measurement of its angular width and lateral expansion (Fig. 2).

The CME height-time profiles extracted along 13 radial slits show a steady outward motion with clear anisotropy: higher-

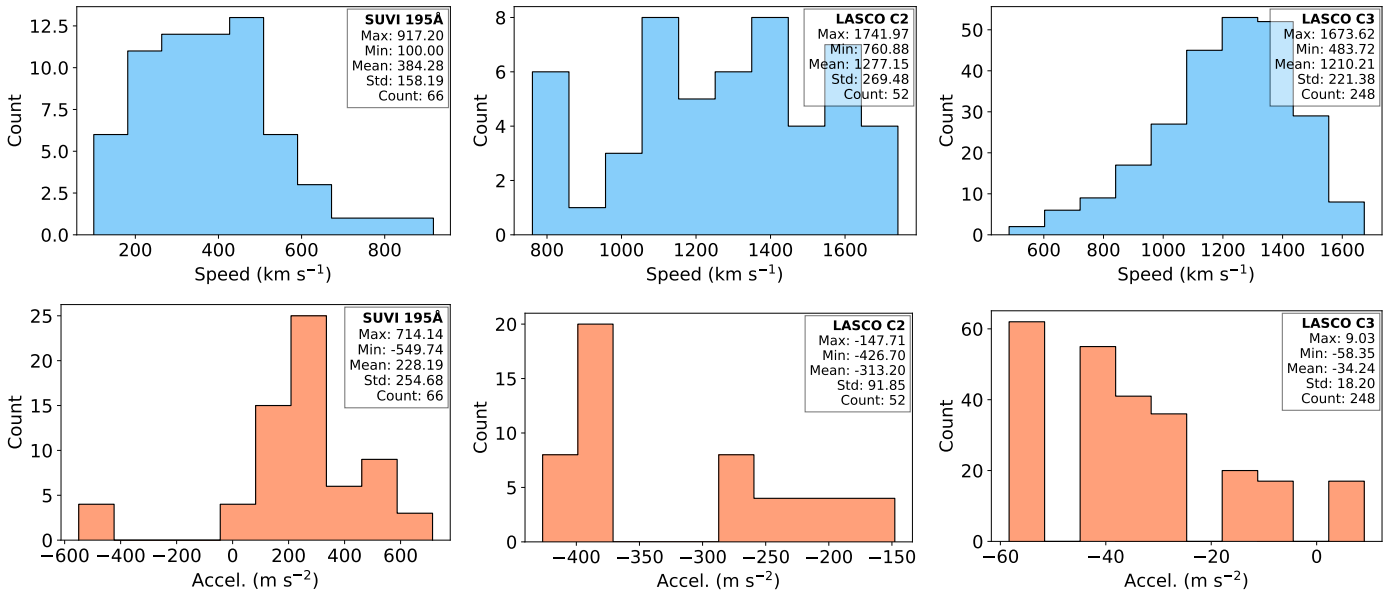
angle slits display slower propagation than lower ones, indicating non-uniform coronal conditions. Derived speeds range from  $\sim 100\text{--}917\text{ km s}^{-1}$  in the SUVI FOV to  $\sim 761\text{--}1742\text{ km s}^{-1}$  in LASCO C2, with acceleration changing from positive near the Sun to predominantly negative higher out, reflecting the transition from impulsive to decelerating phases (Fig. 3). The lateral expansion speed consistently exceeded the radial speed, peaking within the LASCO C2 FOV before stabilising in LASCO C3, confirming an over-expanding CME front in the early phase.

Figure 4 compares the EUV-derived heights with those inferred from the type II burst frequencies, using several electron-density models. Between 17:30 and 17:38 UT, the three-fold and four-fold Newkirk models reproduce the EUV-derived heights most closely, supporting a physical association between the CME-driven shock and the type II radio bursts during that interval. The radio emission ceases after  $\approx 17:45$  UT at a radial distance of about  $3 R_{\odot}$ , while the EUV front first appears in the LASCO C2 FOV at  $\approx 2.78 R_{\odot}$  in the plane of the sky. Although there is a small overlap between the height inferred from the  $4\times$  Newkirk model and the first LASCO C2 height point, this overlap is too limited to draw a conclusive result. Beyond this time, the EUV front continues to expand outwards, reaching  $\approx 6.45 R_{\odot}$  in LASCO C2, which lies beyond the radial range over which the Newkirk formulation remains valid.

For completeness, we also applied the same multiplicative scaling factors used for the Newkirk model to the Saito,



**Fig. 2.** Top panel: Running ratio images showing the EUV wave, as observed by SUVI and LASCO C2 and C3, with the slits defined as position angles. Bottom panel: Temporal evolution of the CME angular width and the triangle’s base, determined by the CME’s widest sector in Fig. 1’s frames.



**Fig. 3.** Distributions of the EUV wave’s speed (top row) and acceleration (bottom row) along the radial slits in Fig. 2 in SUVI (left column), LASCO C2 (middle column), and C3 (right column). The legend boxes represent the statistics for each parameter.

Leblanc, Allen, and Mann density profiles. Although this adjustment shifts the models into the same overall height range, their frequency-height curves still deviate from the EUV-derived shock heights. This behaviour is expected because these analytic density models represent simplified, radial profiles and therefore cannot reflect the event-specific coronal conditions sampled by

the CME front. The scaled Newkirk model, therefore, provides the closest empirical match for this event.

The underestimation of heights by the Leblanc, Mann, Saito, and Allen models—up to  $\approx 1.5$  times—reflects the application of quiet-Sun-derived density models to an active CME environment, whereas the event occurred in a dense active-region

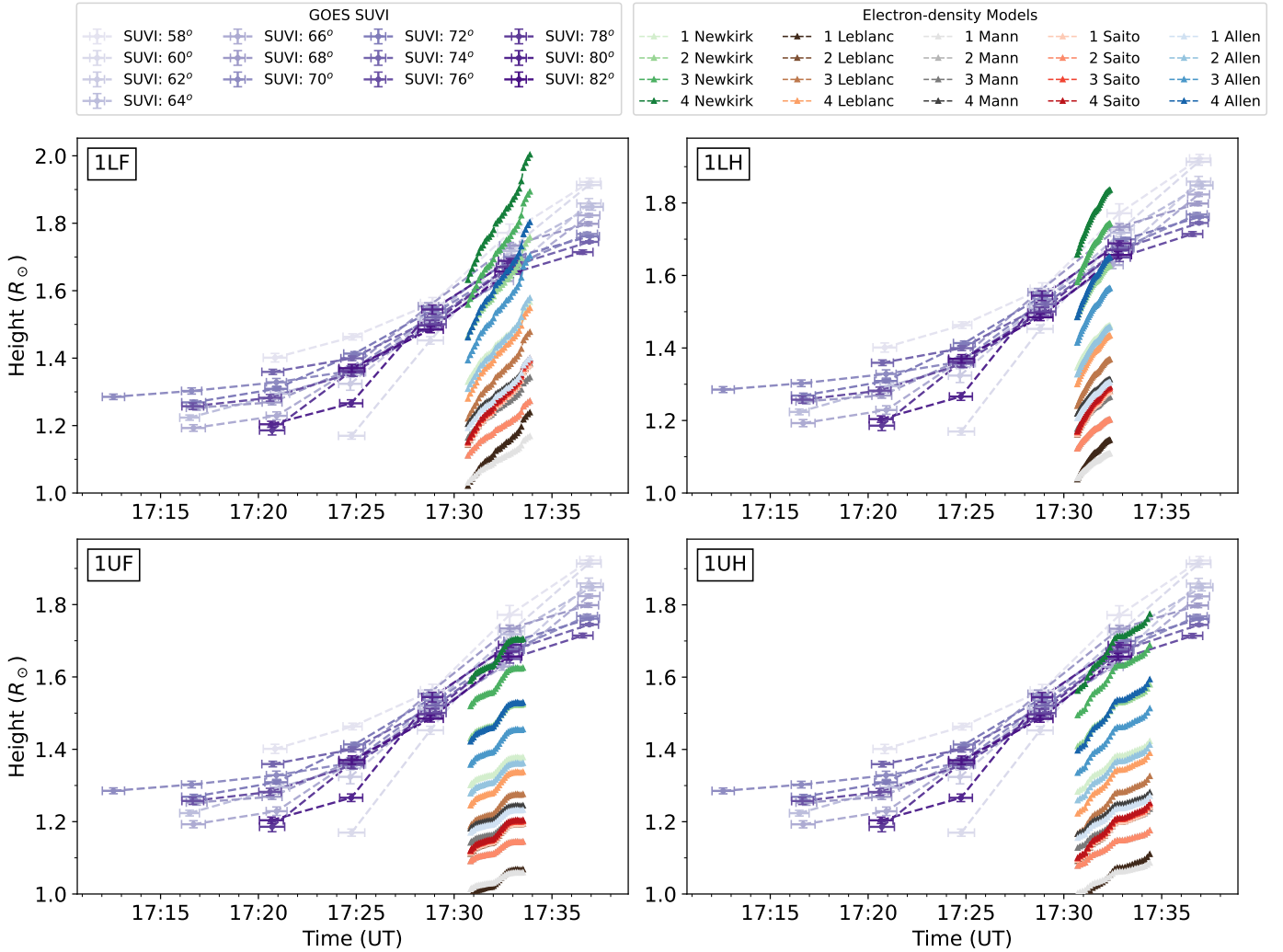


**Fig. 4.** Height-time profile for the coronal wave from SUVI along the slits shown in Fig. 2 and the first type II burst from I-LOFAR, showing different electron density models with a scaling factor from 1 to 4. Left: F lanes. Right: H lanes. Top: Lower lanes. Bottom: Upper lanes. The height-time profiles for the rest of the lanes of type II bursts are listed in Appendix A.

environment. We note that the adoption of a four-fold Newkirk model is empirical and not unique. Similar agreement could be obtained by scaling other density models by appropriate factors. The four-fold Newkirk model is therefore adopted as a representative, but not exclusive, description of the coronal density during this event. We emphasise that the four-fold Newkirk model satisfactorily reproduces only two of the four events, while the remaining cases show noticeable deviations (see Appendices A.1 and A.4).

The remaining offsets between EUV- and model-derived heights likely reflect limitations of the adopted density models and the assumption of a single radial propagation path. Consequently, the correspondence between EUV and modelled radio heights should be regarded as approximate. We explicitly note that, in the absence of radio imaging, these comparisons assume that the radio sources lie close to the plane of the EUV observations, while the actual CME-driven shock is 3D.

Overall, the EUV observations reveal a rapidly accelerating, laterally over-expanding CME that transitions to a more uniform propagation beyond  $\approx 18:00$  UT. The good agreement between the higher-fold Newkirk density models and the EUV heights during the early phase indicates that the type II bursts

were produced by the same CME-driven shock, most likely near its flanks, where coronal densities and magnetic configurations favour efficient shock formation. We note that matching radio-inferred heights to EUV-derived shock fronts assumes the emission originates approximately within the EUV plane of observation. This is an approximation, as the 3D shock geometry may deviate from this plane.

### 3.2. Type II radio bursts

The transient nature of these type II bursts underscores the dynamic interactions between the CME shock and the corona. As the shock propagates, its ability to accelerate particles and produce radio emissions fluctuates with local plasma conditions. This acceleration is particularly efficient when the shock encounters magnetic fields that are quasi-perpendicular to its direction of travel (see e.g. Feng et al. 2012; Kozarev et al. 2017; Kouloumvakos et al. 2021, and references within).

The radio dynamic spectrum, spanning 20–240 MHz, reveal four short-lived and fragmented type II radio bursts between 17:30 and 17:48 UT (Fig. 5). The EUV and white-light running-difference images reveal the CME’s leading edge and its

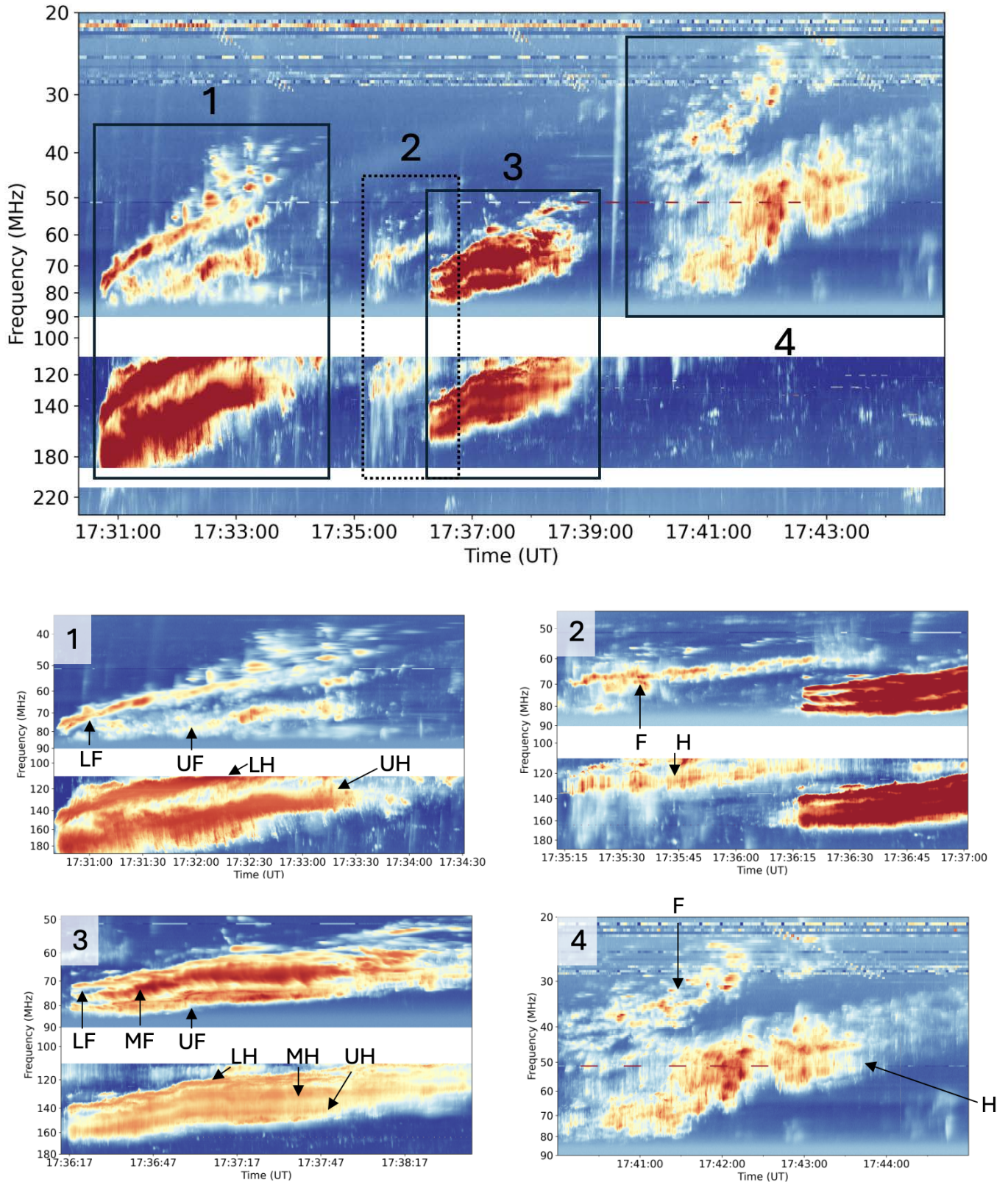


**Fig. 5.** I-LOFAR dynamic spectrum from 17:30 UT to 17:48 UT, covering 20 to 240 MHz, showing emission associated with the second CME. Boxes 1–4 highlight four type II bursts. The last letter in the labels (F or H) indicates whether the emission is fundamental or harmonic. If the label has two letters, it signifies multilane emission or band splitting, with the first letter (L, M, or U) referring to the lower, middle, or upper band, respectively. Each burst exhibits unique spectral features, including band splitting, herringbones, spectral gaps, and fine structures.

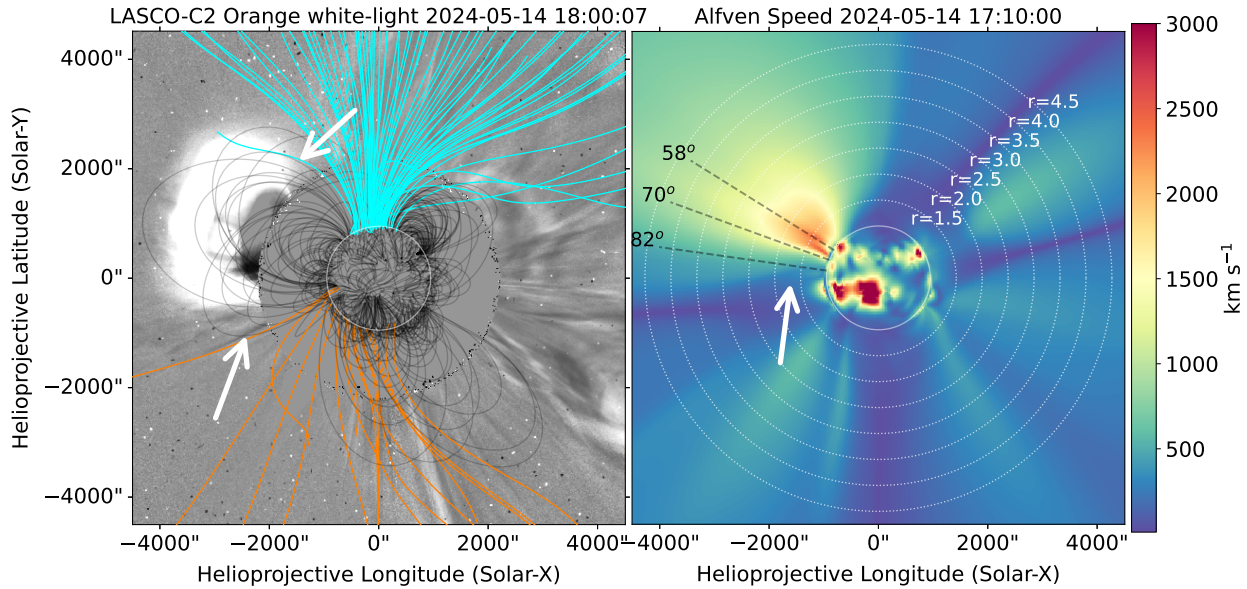


**Fig. 6.** Left: Running ratio image showing the PFSS model on top of the EUV wave in LASCO C2. The cyan and orange lines represent north and south magnetic polarities, respectively. Meanwhile, the black lines represent closed field lines. For better contrast, we used black colours for the closed field lines in the LASCO C2 image. Right: FORWARD maps showing pre-eruption coronal conditions at 17:10 UT. The white circle denotes the solar limb, the same FOV as LASCO C2, with dotted circles representing different radial distances in solar radii. The white arrow points towards the boundary between the CME bottom flank and the streamer where a low Alfvén speed exists, which provides good conditions for shock formation and hence type II radio emissions.

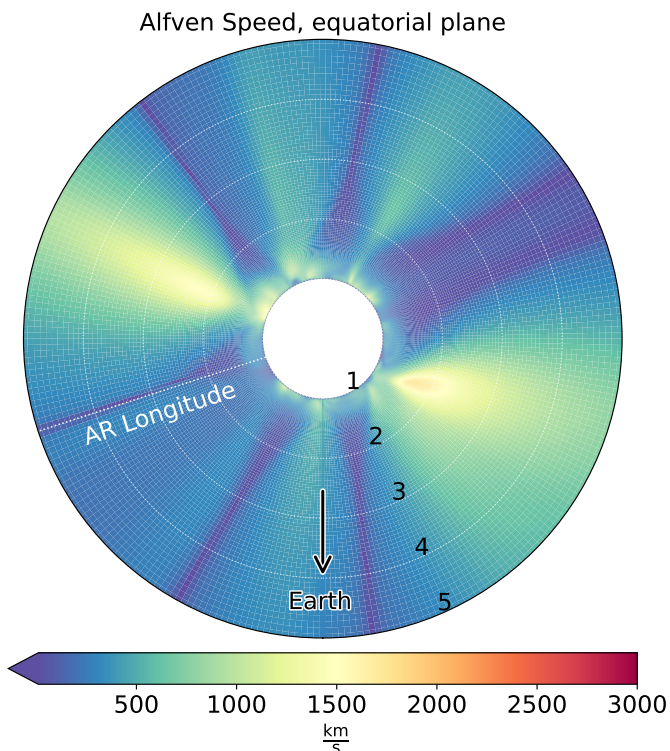


**Fig. 7.** Right: Equatorial cut (top view) showing the CME travelling through a low-Alfvén speed region. See Fig. A.6, which shows the CME in the SUVI FOV travelling towards the north-east.

associated propagating front, which may correspond to a shock wave or a compressed plasma sheath. While these observations do not directly image the radio sources, they indicate the presence of a CME-driven disturbance occurring contemporane-

ously with the bursts, consistent with the conditions required for type II emission. Each type II burst showcases distinctive fine structures, such as F and H lanes, band splitting, herringbones, and fragmented spectra. Notably, the bursts tend to originate at lower frequencies (Table 1), suggesting they were initiated further from the Sun.

The first type II burst, starting at 17:30 UT, displayed both F and H emission bands (Fig. 5). The H emission is significantly brighter, with noticeable fragmentation in both the upper fundamental (UF) and lower fundamental (LF) bands. Herringbones are evident, particularly in the H band, with forward drift herringbones dominating the lower harmonic (LH) and reverse drift herringbones in the upper harmonic (UH). Notably, additional bands appear along the H and F emission lanes between 17:30:00 and 17:31:30 UT. These multiple bands likely result from different parts of the shock front encountering coronal density inhomogeneities, leading to variations in emission properties (e.g. Jebaraj et al. 2020; Tsap et al. 2020). Such interactions can also facilitate particle acceleration along the shock front, contributing to the formation of fine structures in the dynamic spectrum (e.g. Kontar et al. 2017; Magdaleníć et al. 2020; Carley et al. 2021).

The second type II burst, observed between 17:35:15 and 17:36:15 UT, exhibits a weak and fragmented emission. It displays periodic or quasi-periodic packet-like structures, suggesting that MHD waves or shock-induced oscillations may have modulated the emission by periodically compressing and rarefying the plasma, affecting the generation of radio waves (Jebaraj et al. 2020, and references within). Compared to the first burst, its two bands are fainter, more fragmented, and shorter-lived. The fragmentation likely reflects coronal turbulence, which can scatter the radio waves and weaken their intensity (Carley et al. 2021; Koval et al. 2023).

The third type II burst displays a complex spectral structure with multiple well-defined lanes. The burst initially drifted from higher to lower frequencies before, between 17:36 UT

**Table 1.** Characteristics of the type II burst lanes.

| Burst | Band | Start freq<br>(MHz) | End freq<br>(MHz) | Start time<br>(UT) | End time<br>(UT) | Drift rate<br>(kHz s <sup>-1</sup> ) | Radial velocity*<br>(km s <sup>-1</sup> ) | Radial velocity**<br>(km s <sup>-1</sup> ) | Freq ratio<br>(H/F) | Drift ratio<br>(H/F) |
|-------|------|---------------------|-------------------|--------------------|------------------|--------------------------------------|---|--|---------------------|----------------------|
| 1     | LF   | 77.61               | 44.07             | 17:30:42           | 17:33:52         | -157.48                              | 1227.51                                   | 755.77                                     | 2.29                | 2.15                 |
|       | LH   | 148.14              | 110.55            | 17:30:41           | 17:32:22         | -361.30                              | 1224.16                                   | 936.87                                     |                     |                      |
|       | UF   | 84.28               | 68.03             | 17:30:48           | 17:33:31         | -107.42                              | 546.37                                    | 450.05                                     |                     |                      |
|       | UH   | 177.81              | 121.39            | 17:30:42           | 17:34:24         | -239.77                              | 632.60                                    | 460.30                                     |                     |                      |
| 2     | F    | 68.90               | 57.98             | 17:35:16           | 17:36:38         | -121.64                              | 810.06                                    | 712.09                                     | 1.86                | 1.91                 |
|       | H    | 130.54              | 114.50            | 17:35:16           | 17:36:27         | -226.21                              | 816.65                                    | 725.51                                     |                     |                      |
| 3     | LF   | 71.80               | 59.58             | 17:36:18           | 17:38:40         | -85.04                               | 553.15                                    | 464.55                                     | 2.35                | 1.91                 |
|       | LH   | 139.48              | 111.05            | 17:36:17           | 17:38:40         | -200.22                              | 709.25                                    | 574.23                                     |                     |                      |
|       | MF   | 75.86               | 64.81             | 17:36:18           | 17:38:39         | -77.88                               | 443.09                                    | 388.16                                     |                     |                      |
|       | MH   | 150.05              | 125.63            | 17:36:17           | 17:38:38         | -161.54                              | 480.89                                    | 410.04                                     |                     |                      |
|       | UF   | 80.99               | 68.18             | 17:36:18           | 17:38:39         | -97.43                               | 497.91                                    | 435.79                                     |                     |                      |
|       | UH   | 159.90              | 133.10            | 17:36:17           | 17:38:16         | -216.04                              | 568.12                                    | 493.56                                     |                     |                      |
| 4     | F    | 41.07               | 26.10             | 17:40:03           | 17:43:19         | -85.85                               | 1939.38                                   | 1243.59                                    | 1.52                | 1.68                 |
|       | H    | 74.44               | 38.49             | 17:40:04           | 17:44:56         | -130.21                              | 2075.31                                   | 1131.06                                    |                     |                      |

**Notes.** The band labels here are the same used in Fig. 5, with the number signifying the four type II bursts to which the band belongs. The start and end points given are the mean frequency and time values from ten manual attempts to click on the first and last points on the burst lane. In all bursts except burst 4, the F emission began later than the H emission. The drift rate is the slope of the burst obtained via linear regression of the mean points. The radial velocities are estimated by two methods: the first method is by fitting the deduced radial distances from the 4× Newkirk model over time, and the second method is by using the drift rates (Morosan et al. 2019). The Alfvén Mach number is the mean value estimated from the band-splitting method. The start and end times are rounded to the nearest second for clarity. Uncertainties range from 0.02–0.61 MHz for start frequencies, 0.04–0.54 MHz for end frequencies, 27–903 ms for start times, and 59–446 ms for end times. \* Radial velocity from the first method. \*\* Radial velocity from the second method.

**Table 2.** Mach numbers calculated from band splitting between H and F pairs.

|               |               |               |               |
|---------------|---------------|---------------|---------------|
| 1UH/1LH: 3.35 | 1UF/1LF: 3.57 | 3UH/3MH: 3.23 | 3MH/3LH: 3.24 |
| 3UH/3LH: 3.46 | 3UF/3MF: 3.21 | 3MF/3LF: 3.21 | 3UF/3LF: 3.41 |

and 17:37 UT, transitioning into a nearly stationary state as the spectral lanes flattened (i.e. for the F band:  $-0.04$ ,  $-0.03$ , and  $-0.08$  MHz s<sup>-1</sup> for LF, MF, and UF lanes, respectively. For the H band:  $-0.11$ ,  $-0.06$ , and  $-0.19$  MHz s<sup>-1</sup> for LH, MH, and UH lanes, respectively). These values are the mean drift rates, calculated by Savitzky-Golay fitting, between 17:37:01–17:38:40 UT. This behaviour is opposite to that reported by Chrysaphi et al. (2020), where a stationary burst evolved into a drifting one. The physical origin of the band splitting observed in this event remains uncertain and may reflect one or more of several possible scenarios.

One interpretation suggests that the emission arises simultaneously from the upstream and downstream regions of the shock front, representing two nearly co-spatial sources separated by the density jump across the shock (Smerd et al. 1975; Chrysaphi et al. 2018). Alternatively, non-thermal electrons accelerated in the upstream region may penetrate into the downstream plasma, where they generate Langmuir waves responsible for the split-band emission (Bale et al. 1999; Thejappa & MacDowall 2000). Another possibility is that the band-split emission originates from quasi-perpendicular regions of the shock front where collapsing magnetic trap geometries facilitate efficient electron acceleration (Magdalenic et al. 2002). It has also been proposed that the two bands may correspond to spatially distinct regions along the shock surface encountering different local plasma densities or magnetic field configurations (Holman & Pesses 1983; Bhunia et al. 2023).

Interestingly, the F bands of the third type II burst (3LF, 3MF, and 3UF) are brighter than their high-frequency counterparts. This may arise from differences in coronal conditions. As the shock propagates and weakens through expansion and interaction, both its acceleration efficiency and its ability to generate Langmuir waves decline, either due to energy loss or encounters with more parallel magnetic fields, leading to reduced backbone brightness (Maguire et al. 2020).

The fourth type II burst appears notably fragmented but a clear connection between its F and H components remain evident despite its irregular structure. This fragmentation is likely influenced by turbulence and scattering, highlighting the dynamic nature of shock-corona interactions during the CME. The two bands of this burst are more fragmented and have a longer duration compared to earlier bursts. This burst also exhibits scattered blobs of intensity within its fragmented bands, which may result from scattering effects as the radio emissions propagate through density inhomogeneities in the coronal plasma. Reverse drifts in the herringbone structures indicate electrons being accelerated towards the Sun or through a denser plasma, further underscoring the localised and dynamic plasma conditions.

Only burst 3 shows clear evidence of band splitting. However, for bursts 1, 2, and 4, multiple lanes were present but not consistent with standard band-splitting signatures.

The characteristics of the type II burst lanes are presented in Tables 1 and 2, which offer a comprehensive examination of the key properties of these radio burst lanes. The type II burst lanes exhibited notable variations in their start and end frequencies, ranging from  $\sim 41$  MHz to  $\sim 178$  MHz. Particularly interesting is the observed temporal offset between the F and H emissions. In the first three bursts, the F component began 1 to 6 seconds later than the H component. The end times of the F and H bands also exhibited larger disparities, perhaps due to variations in the local plasma environment and the evolving shock wave structure.

Mean frequency ratio and mean drift ratio were calculated for each H and F pair. The drift rates of the radio burst lanes demonstrate significant variability, ranging from  $\sim -361 \text{ kHz s}^{-1}$  to  $-78 \text{ kHz s}^{-1}$ . Notably, the radial velocities associated with the drift rates vary considerably, from almost  $443 \text{ km s}^{-1}$  to  $2075 \text{ km s}^{-1}$ . The F and H band pairs exhibit frequency ratios predominantly close to the theoretical value of 2, with observed ratios ranging from 1.52 to 2.35. These results are in agreement with the results reported by Mann et al. (1996).

Burst 4 exhibits stronger fragmentation and the highest radial velocities among the four observed bursts, reaching approximately  $1939 \text{ km s}^{-1}$  for the F band and  $2075 \text{ km s}^{-1}$  for the H band. These comparatively high speeds likely reflect variations in the local plasma environment or differences in shock dynamics at the time of emission. The observed characteristics remain consistent with existing theoretical models of solar type II radio burst propagation. The near-theoretical drift-rate ratios and the delayed onset of the F emission support the current understanding of plasma-wave interactions and radio-wave propagation effects in eruptive environments. However, the variability in drift rates between bursts indicates evolving coronal conditions and warrants further investigation into how local plasma parameters and energy-transfer processes influence the observed emission properties.

For the Mach number estimates, the two methods yield systematically different Mach numbers. The band-splitting values range between 3.21–3.57 (Table 1). These represent local shock conditions at the type II emission site, whereas the CME-speed-based values range between 0.06–1.24 (Fig. A.6). These reflect the global expansion of the CME front and depend on the FORWARD-derived Alfvén speed. Because the radio-emitting shock patch does not necessarily correspond to the region sampled by the CME leading edge, and because the FORWARD model describes the background corona rather than the immediate shock vicinity, numerical differences between the two estimates are expected.

#### 4. Discussion

To interpret the radio and EUV signatures of the eruption, we analysed the event within the broader framework of CME-driven shock dynamics, coronal magnetic field configurations, and plasma properties derived from both observations and physics-driven modelling. The radio emissions of the type II bursts exhibit F and H components, with a multilane structure in each band. This multi-channel morphology likely results from the CME shock wave encountering adjacent streamer-type formations (Lv et al. 2017; Chrysaphi et al. 2018). The observation that different lanes have different frequency drifts is likely due to different source locations along the shock and different structures involved. Lv et al. (2017) demonstrated that multiple type II lanes with different drifts can be generated even though the burst is associated with a single CME.

During lateral propagation, the CME undergoes significant interaction with neighbouring coronal features, particularly streamers, which possess enhanced density compared to the ambient medium and consequently exhibit reduced characteristic Alfvén velocities. These conditions promote shock wave development or amplification of existing shock structures as they traverse these regions. Furthermore, the shock geometry may become quasi-perpendicular along the lateral boundaries. These combined mechanisms facilitate effective particle acceleration and type II radio emission generation at the shock front (e.g. Claßen & Aurass 2002; Mancuso & Raymond 2004; Zucca et al. 2014; Lv et al. 2017).

The discrepancy between the EUV- and model-derived heights persists throughout the type II burst interval, reflecting the inherent limitations of 1D coronal density models when applied to complex CME geometries. These models assume a simple, radially stratified corona, whereas CME-driven shocks are extended 3D structures that often propagate obliquely to the radial direction. The restricted temporal overlap between the EUV and radio observations, combined with the breakdown of low-corona density formulations at longer heliocentric distances, further limits the accuracy of frequency-to-height conversions. Consequently, the mismatch should not be viewed as a failure of the modelling approach but rather as an indication of its restricted applicability. Such comparisons nonetheless remain useful for providing first-order constraints on the likely height range of type II radio sources and for establishing their temporal correspondence with EUV-observed shocks.

The density models proposed by Leblanc, Mann, Saito, and Allen show limited applicability for characterising all observed emission lanes in the current investigation. Only the three- and four-fold Newkirk density models match the height at which the type II bursts originated at those specific frequencies. A similar analysis was presented by Kouloumvakos et al. (2014), which enables direct comparison with the trends observed here.

We also estimated the CME lateral speed and the CME's angular width in the FOV of the three instruments (Fig. 2) by fitting a curved triangle to the CME leading edge in the running-ratio images shown in Fig. 1. We find that the expansion speed is higher than the radial speed, in general. The CME accelerated in the SUVI FOV, with the expansion speed peaking in the LASCO C2 FOV and becoming more stable in the LASCO C3 FOV. The lateral-to-radial speed ratio suggests an over-expanding CME front during the early and intermediate phases, possibly driven by strong magnetic pressure gradients or rapid reconfiguration of overlying coronal structures. The peaking of the expansion speed in the LASCO C2 FOV indicates that the lateral forces dominate early on before stabilising, as the CME enters the more radial regime observed by LASCO C3.

To explore the global structure of the coronal magnetic field during the eruption, we combined observational data with modelling by applying magnetogram data from the Global Oscillation Network Group (GONG) (Harvey et al. 1996) in the potential field source surface (PFSS) model. We defined a grid of footpoints on the GONG map over the Sun-facing side visible from Earth. These footpoints served as seed points for tracing coronal magnetic field lines using the Python package *pfsspy*<sup>2</sup>, which provides a robust implementation of the PFSS model described by Stansby et al. (2020). In Fig. 6, we show running-ratio images of the eruption captured by SUVI and LASCO C2, overlaid with the modelled magnetic field lines.

To analyse the coronal plasma conditions before the eruption, we used the Predictive Science Inc. (PSI) standard coronal solutions obtained from MHD simulations based on the MAS model results (Mikić et al. 1999). We accessed and retrieved these datasets for 2024 May 14 at 17:10 UT using the FORWARD toolset (Gibson et al. 2016). This tool allowed us to produce 2D maps of plasma properties derived from the MAS model results. In Fig. 6, we present a FORWARD-generated map of the Alfvén speed, as well as the extrapolated coronal magnetic field from the PFSS model in the LASCO C2 FOV.

To better understand the coronal environment upon the eruption, we extrapolated the coronal magnetic field via the PFSS model and show the field lines overlaid on the running-ratio EUV

<sup>2</sup> Pfsspy tool: <https://pfsspy.readthedocs.io/>

and white-light observations from SUVI and LASCO C2, respectively, in Fig. 6. The shock wave appears as a bright structure at the eastern solar limb, with the magnetic field configuration indicating a highly structured and anisotropic coronal environment. The cyan and orange lines in Fig. 6 represent open field lines directed away from and towards the Sun, respectively. Meanwhile, the black lines represent closed field lines. Notably, the shock front aligns closely with regions of closed magnetic field concentration, with the shock shoulders near the open field lines on both flanks, which could play a significant role in particle acceleration processes and the generation of type II radio bursts.

We inspected a suite of 2D parameter maps derived from the MAS model, using the FORWARD toolset, including electron density, magnetic field strength, Alfvén speed, plasma beta, total pressure, and temperature, integrated along the line of sight and projected onto the plane of the sky. The white circle at the centre marks the edge of the Sun in EUV. While only the Alfvén speed map is shown (Fig. 6), the full set of maps provides the physical context for the observed shock structure (Fig. A.5). The density and magnetic field maps show typical coronal trends, with values decreasing with height, and enhanced density along the bottom shock flank, in particular. This is likely to align with the source region of the type II bursts. Elevated temperature and pressure along the shock front further support its compressive and heating effects on the surrounding plasma.

After comparing the mean CME speed along each slit with the radial speed of each type II lane deduced from 4× Newkirk density model, we found that the closest match between the CME speed and the type II bursts is near the CME’s flanks, with the majority of the match at the upper flank. This observation disagrees with the standard assumption that type II emissions form exclusively in regions of low Alfvén speed, as seen in Fig. 6, but remains consistent with the interpretation that radio emissions can arise from localised variations in the coronal density structure. However, the FORWARD map here is the integrated Alfvén speed along the line of sight, which can obscure localised minima in Alfvén speed along the CME flank where the radio emission is generated. So, we checked the distribution of the Alfvén speed in the equatorial plane to find a void in the corona with a low Alfvén speed near the active region location where the CME was launched (Fig. 7). As expected, we saw that the CME indeed travelled through a region of relatively low Alfvén speed.

However, this apparent agreement between the CME speed and the radial speed for the type II bursts does not necessarily indicate that the radio emissions originated from the CME upper flank. The derived radio source heights depend strongly on the choice of coronal density model, which assumes an idealised, radially symmetric corona, whereas the real coronal environment is highly structured. Additional uncertainties arise from projection effects and the limited spatial coverage of the observations, which can obscure the true 3D geometry of the shock front.

Therefore, while the kinematic comparison suggests an apparent match along the upper flank, this result should be interpreted with caution. The lack of radio imaging and the limitations of 1D density models prevent a definitive identification of the emission site. This interpretation is supported by the low Alfvén speed co-spatial with the streamer in the FORWARD map (Fig. 6) and the large-scale magnetic topology of the region (Fig. 7).

The PFSS model shows the shock as expanding closed coronal loops with open field lines at the flanks and shoulders, likely associated with the generation of type II radio bursts. The FORWARD maps reveal regions of enhanced density, low Alfvén speed, and elevated plasma beta at these locations, supporting

their role in shock-induced radio wave production. These findings highlight the connection between the shock’s structure and the coronal environment, providing insight into the conditions facilitating particle acceleration and radio emission.

The discrepancy between the Mach numbers in Table 1 and those shown in Appendix A arises naturally from the different techniques employed. Band splitting directly samples the density jump at the radio-emitting shock segment and therefore measures the local compression. In contrast, the CME-speed-based Mach numbers use a model-derived Alfvén speed and the bulk CME kinematics, which characterise a different portion of the shock surface. Given the spatially structured nature of CME-driven shocks and the sensitivity of both methods to different physical inputs, exact agreement is not expected. The values presented here should therefore be interpreted as complementary diagnostics rather than inconsistent measurements. However, the results are consistent with those reported in previous works (e.g. Maguire et al. 2021; Zucca et al. 2014; Maguire et al. 2020; Kouloumvakos et al. 2021; Su et al. 2022; Vasanth 2025).

## 5. Conclusions

In this work, we used high-resolution I–LOFAR spectroscopic observations of four type II radio bursts linked to a CME event on 2024 May 14. We explored the relationship between solar radio emissions and CMEs through an in-depth analysis of I–LOFAR dynamic spectra, complemented by EUV and white-light observations from SUVI and LASCO instruments to investigate the CME’s kinematics.

The type II bursts exhibited distinct spectral features, including multi-lane band splitting, herringbones, and spectral fragmentation. These features point to transient interactions between shocks and the solar corona, with emission characteristics shaped by varying plasma conditions and magnetic field configurations. The delayed appearance of F emissions compared to H emissions, along with observed drift rates, aligns with models of plasma emission processes, density irregularities, and the effects of wave propagation in the corona.

The absence of radio imaging data prevented us from pinpointing the exact origins of the type II bursts, making it challenging to establish a direct connection between the radio sources and specific CME structures. However, some type II emissions originated from heights observable by SUVI. By analysing the height-time profiles of both the type II bursts and the CME’s leading edge, we inferred a correlation between the two. Furthermore, using modelled coronal parameters, we estimated that the type II bursts likely originated from the interaction between the lower CME flank and the coronal streamer at the east limb, where reduced Alfvén speeds may have facilitated their generation. Future studies incorporating improved radio imaging coverage and enhanced observational techniques are necessary to advance our understanding of the physical conditions of CME-driven type II emissions.

The shock wave’s anisotropic expansion, varying velocities, and accelerations reflect the influence of non-uniform coronal densities and magnetic field strengths. The comparison between EUV-derived shock heights and radio source-inferred distances confirms a strong correlation, especially with 3× and 4× Newkirk density models in the later stages of the CME’s propagation in the SUVI FOV. However, deviations at later times emphasize the need for refined coronal density models at greater heights.

Therefore, this investigation demonstrates that determining the spatial origin of type II radio sources presents significant

challenges in the absence of direct source imaging. Here, we leveraged the EUV imaging data as well as the MAS and PFSS model results to constrain the likely location of the type II radio source. This highlights the necessity of direct-imaging data at radio wavelengths to unravel the secrets of the type II origin.

The Alfvén Mach numbers obtained from band splitting and from CME-speed-based estimates probe different portions of the shock and rely on different physical assumptions. As a result, their numerical values differ, reflecting methodological differences rather than inconsistencies in the event.

This study sheds light on the complex processes underlying type II radio bursts and their links to CME-driven shock waves. The findings highlight the importance of integrating multi-wavelength data with theoretical models to unravel the dynamics of solar eruptions. Future work should prioritise continuous, high-resolution solar radio imaging, refine density models, and investigate 3D CME structures to address current uncertainties and deepen our knowledge of shock-plasma interactions in the solar corona.

*Acknowledgements.* We would like to thank the referee for the valuable feedback. We acknowledge the support from the I-LOFAR Chief Observers (CO) team. Data is provided by the I-LOFAR station, supported by Science Foundation Ireland. We acknowledge using data from the GOES/SUVI and SOHO/LASCO instruments. We acknowledge using the sunpy Python package (The SunPy Community 2020) for data visualisation. Thanks to Jeremy Rigney for helping with the radio dynamic spectrum. Thanks to Laura Hayes and Shane Maloney for the helpful discussions. Thanks to Kamen Kozarev for helping with the FORWARD map. We acknowledge using the psipy package for plotting the PSI-MAS data (<https://psipy.readthedocs.io/>). We also acknowledge using pieces of code from Zhang et al. (2018)'s repository (<https://github.com/peijin94/type3detect/tree/master>). This work is supported by the project "The Origin and Evolution of Solar Energetic Particles", funded by the European Office of Aerospace Research and Development under award No. FA8655-24-1-7392.

## References

- Abidin, Z. Z., Zulkiplee, A. N., Epin, V., & Pauzi, F. A. M. 2023, *RAA*, **23**, 055010
- Allen, C. W. 1947, *MNRAS*, **107**, 426
- Bale, S. D., Reiner, M. J., Bougeret, J. L., et al. 1999, *Geophys. Res. Lett.*, **26**, 1573
- Bhunia, S., Carley, E. P., Oberoi, D., & Gallagher, P. T. 2023, *A&A*, **670**, A169
- Byrne, J. P., Long, D. M., Gallagher, P. T., et al. 2013, *A&A*, **557**, A96
- Carley, E. P., Cecconi, B., Reid, H. A., et al. 2021, *ApJ*, **921**, 3
- Chernov, G., & Fomichev, V. 2021, *ApJ*, **922**, 82
- Chrysaphi, N., Kontar, E. P., Holman, G. D., & Temmer, M. 2018, *ApJ*, **868**, 79
- Chrysaphi, N., Reid, H. A. S., & Kontar, E. P. 2020, *ApJ*, **893**, 115
- Claßen, H. T., & Aurass, H. 2002, *A&A*, **384**, 1098
- Downs, C., Roussev, I. I., van der Holst, B., Lugaz, N., & Sokolov, I. V. 2012, *ApJ*, **750**, 134
- Feng, S. W., Chen, Y., Kong, X. L., et al. 2012, *ApJ*, **753**, 21
- Frassati, F., Susino, R., Mancuso, S., & Bemporad, A. 2019, *ApJ*, **871**, 212
- Gallagher, P. T., Lawrence, G. R., & Dennis, B. R. 2003, *ApJ*, **588**, L53
- Gibson, S. E., Kucera, T. A., White, S. M., et al. 2016, *Front. Astron. Space Sci.*, **3**, 8
- Harvey, J. W., Hill, F., Hubbard, R. P., et al. 1996, *Science*, **272**, 1284
- Holman, G. D., & Pesses, M. E. 1983, *ApJ*, **267**, 837
- Jarry, M., Rouillard, A. P., Plotnikov, I., Kouloumvakos, A., & Warmuth, A. 2023, *A&A*, **672**, A127
- Jebaraj, I. C., Magdalenic, J., Podladchikova, T., et al. 2020, *A&A*, **639**, A56
- Kilpua, E., Koskinen, H. E. J., & Pulkkinen, T. I. 2017, *Liv. Rev. Sol. Phys.*, **14**, 5
- Knock, S. A., & Cairns, I. H. 2005, *J. Geophys. Res.: Space Phys.*, **110**, A01101
- Kong, X. L., Chen, Y., Li, G., et al. 2012, *ApJ*, **750**, 158
- Kontar, E. P., Yu, S., Kuznetsov, A. A., et al. 2017, *Nat. Commun.*, **8**, 1515
- Kouloumvakos, A., Patsourakos, S., Hillaris, A., et al. 2014, *Sol. Phys.*, **289**, 2123
- Kouloumvakos, A., Rouillard, A., Warmuth, A., et al. 2021, *ApJ*, **913**, 99
- Koval, A., Stanislavsky, A., Karlický, M., et al. 2023, *ApJ*, **952**, 51
- Kozarev, K. A., Raymond, J. C., Lobzin, V. V., & Hammer, M. 2015, *ApJ*, **799**, 167
- Kozarev, K. A., Davey, A., Kendrick, A., Hammer, M., & Keith, C. 2017, *J. Space Weather Space Clim.*, **7**, A32
- Kozarev, K., Nedal, M., Miteva, R., Dechev, M., & Zucca, P. 2022, *Front. Astron. Space Sci.*, **9**, 801429
- Kumari, A., Morosan, D. E., Kilpua, E. K. J., & Daei, F. 2023, *A&A*, **675**, A102
- Leblanc, Y., Dulk, G. A., & Bougeret, J.-L. 1998, *Sol. Phys.*, **183**, 165
- Li, X., Xiang, Z., Mei, Y., et al. 2025, *J. Geophys. Res.: Space Phys.*, **130**, e2024JA033504
- Liu, Y., Luhmann, J. G., Bale, S. D., & Lin, R. P. 2011, *ApJ*, **734**, 84
- Long, D. M., Gallagher, P. T., McAtteer, R. T. J., & Bloomfield, D. S. 2008, *ApJ*, **680**, L81
- Long, D. M., DeLuca, E. E., & Gallagher, P. T. 2011, *ApJ*, **741**, L21
- Long, D. M., Murphy, P., Graham, G., Carley, E. P., & Pérez-Suárez, D. 2017, *Sol. Phys.*, **292**, 185
- Long, D. M., Jenkins, J., & Valori, G. 2019, *ApJ*, **882**, 90
- Lulić, S., Vršnak, B., Žic, T., et al. 2013, *Sol. Phys.*, **286**, 509
- Lv, M. S., Chen, Y., Li, C. Y., et al. 2017, *Sol. Phys.*, **292**, 194
- Magdalenic, J., Vršnak, B., & Aurass, H. 2002, *ESA Spec. Publ.*, **1**, 335
- Magdalenic, J., Marqué, C., Fallows, R. A., et al. 2020, *ApJ*, **897**, L15
- Maguire, C. A., Carley, E. P., McCauley, J., & Gallagher, P. T. 2020, *A&A*, **633**, A56
- Maguire, C. A., Carley, E. P., Zucca, P., Vilmer, N., & Gallagher, P. T. 2021, *ApJ*, **909**, 2
- Mancuso, S., & Raymond, J. C. 2004, *A&A*, **413**, 363
- Mann, G., Classen, T., & Aurass, H. 1995, *A&A*, **295**, 775
- Mann, G., Klassen, A., Classen, H.-T., et al. 1996, *A&AS*, **119**, 489
- Mann, G., Jansen, F., MacDowall, R. J., Kaiser, M. L., & Stone, R. G. 1999, *A&A*, **348**, 614
- Mann, G., Vocks, C., Warmuth, A., et al. 2022, *A&A*, **660**, A71
- Mikić, Z., Linker, J. A., Schnack, D. D., Lionello, R., & Tarditi, A. 1999, *Phys. Plasmas*, **6**, 2217
- Morosan, D. E., Carley, E. P., Hayes, L. A., et al. 2019, *Nat. Astron.*, **3**, 452
- Morosan, D. E., Pomoell, J., Kumari, A., Kilpua, E. K. J., & Vainio, R. 2023, *A&A*, **675**, A98
- Murphy, P. C., Callanan, P., McCauley, J., et al. 2021, *A&A*, **655**, A16
- Nedal, M., Mahrous, A., & Youssef, M. 2019, *Ap&SS*, **364**, 161
- Nedal, M., Kozarev, K., Miteva, R., Stepanyuk, O., & Dechev, M. 2024, *Bulg. Astron. J.*, **41**, 63
- Nedal, M., Long, D. M., Cuddy, C., Van Driel-Gesztelyi, L., & Gallagher, P. T. 2025, *A&A*, **695**, L24
- Newkirk, G. 1961, *ApJ*, **133**, 983
- Nitta, N. V., Schrijver, C. J., Title, A. M., & Liu, W. 2013, *ApJ*, **776**, 58
- Patsourakos, S., & Vourlidas, A. 2012, *Sol. Phys.*, **281**, 187
- Raja, K. S., Rabi, A. B., Ingadottir, B., et al. 2023, *An Overview of Solar Radio Type II Bursts through analysis of associated solar and near Earth space weather features during Ascending phase of SC 25*
- Ramesh, R., Kathiravan, C., & Kumari, A. 2023, *ApJ*, **943**, 43
- Saito, K., Makita, M., Nishi, K., & Hata, S. 1970, *Ann. Tokyo Astron. Obs.*, **12**, 51
- Smerd, S. F., Sheridan, K. V., & Stewart, R. T. 1975, *Astrophys. Lett.*, **16**, 23
- Song, H. Q., Zhang, J., Li, L. P., et al. 2019, *ApJ*, **887**, 124
- Song, H., Li, L., Zhou, Z., et al. 2023, *ApJ*, **952**, L22
- Stansby, D., Yeates, A., & Badman, S. T. 2020, *J. Open Source Softw.*, **5**, 2732
- Su, W., Li, T. M., Cheng, X., et al. 2022, *ApJ*, **929**, 175
- The SunPy Community (Barnes, W. T., et al.) 2020, *ApJ*, **890**, 68
- Thejappa, G., & MacDowall, R. J. 2000, *ApJ*, **544**, L163
- Toida, M., & Urugami, T. 2013, *Phys. Plasmas*, **20**, 112302
- Tsap, Y. T., Isaeva, E. A., & Kopylova, Y. G. 2020, *Astron. Lett.*, **46**, 144
- Tsurutani, B. T., & Lakhina, G. S. 2014, *Geophys. Res. Lett.*, **41**, 287
- van Haarlem, M. P., Wise, M. W., Gunst, A. W., et al. 2013, *A&A*, **556**, A2
- Vasanth, V. 2025, *Sci. Rep.*, **15**, 34279
- Vourlidas, A. 2014, *Plasma Phys. Control. Fusion*, **56**, 064001
- Vourlidas, A., & Bemporad, A. 2012, *AIP Conf. Ser.*, **1436**, 279
- Vršnak, B., Aurass, H., Magdalenic, J., & Gopalswamy, N. 2001, *A&A*, **377**, 321
- Vršnak, B., Magdalenic, J., Aurass, H., & Mann, G. 2002, *A&A*, **396**, 673
- Zhang, P., Wang, C. B., & Ye, L. 2018, *A&A*, **618**, A165
- Zhang, P., Morosan, D. E., Zucca, P., et al. 2024, *A&A*, **684**, L22
- Zimovets, I., & Sadykov, V. 2015, *Adv. Sol. Phys.*, **56**, 2811
- Zimovets, I., Vilmer, N., Chian, A. C. L., Sharykin, I., & Struminsky, A. 2012, *A&A*, **547**, A6
- Zucca, P., Carley, E. P., Bloomfield, D. S., & Gallagher, P. T. 2014, *A&A*, **564**, A47
- Zucca, P., Pick, M., Démoulin, P., et al. 2014, *ApJ*, **795**, 68

**Appendix A: Supplementary figures**

Figure A.6 shows another method to estimate the Alfvén Mach number as the ratio between the traced CME speed in the SUVI FOV and the sampled Alfvén speed from the FORWARD map. The top-right zoomed-in panel reveals the pixelated grid, which explains the jagged-looking red curve of the sampled Alfvén speed in the bottom panels.

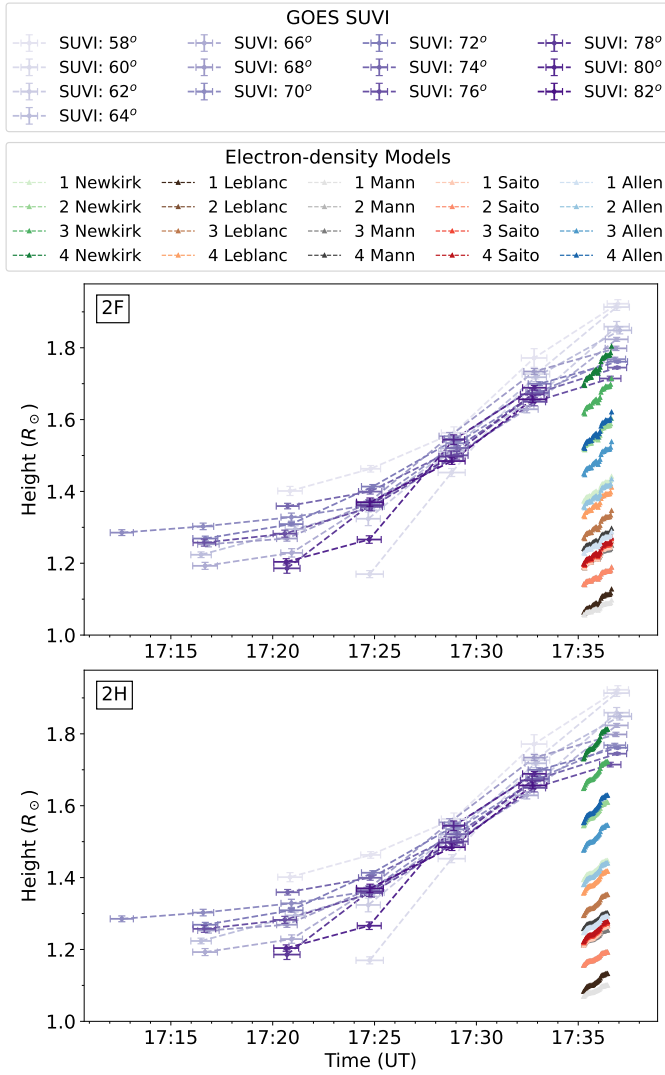


**Fig. A.1.** Second type II burst.

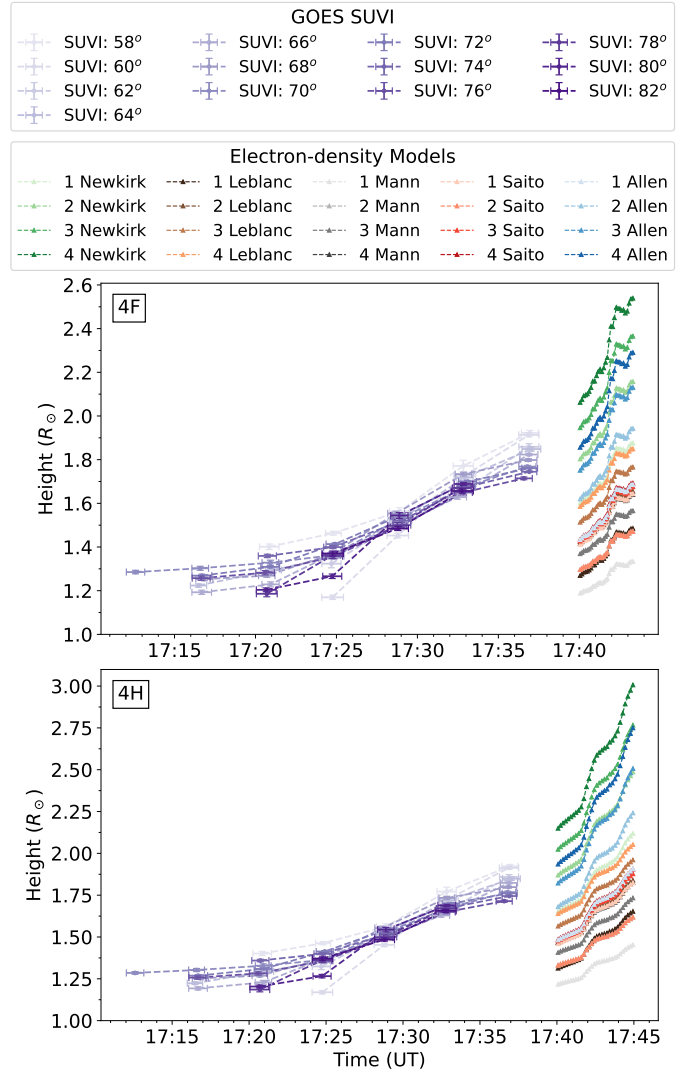


**Fig. A.2.** Fourth type II burst.

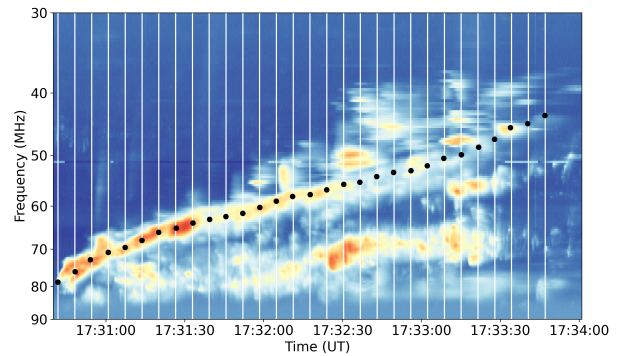


**Fig. A.3.** Clicked points for burst 1LF.

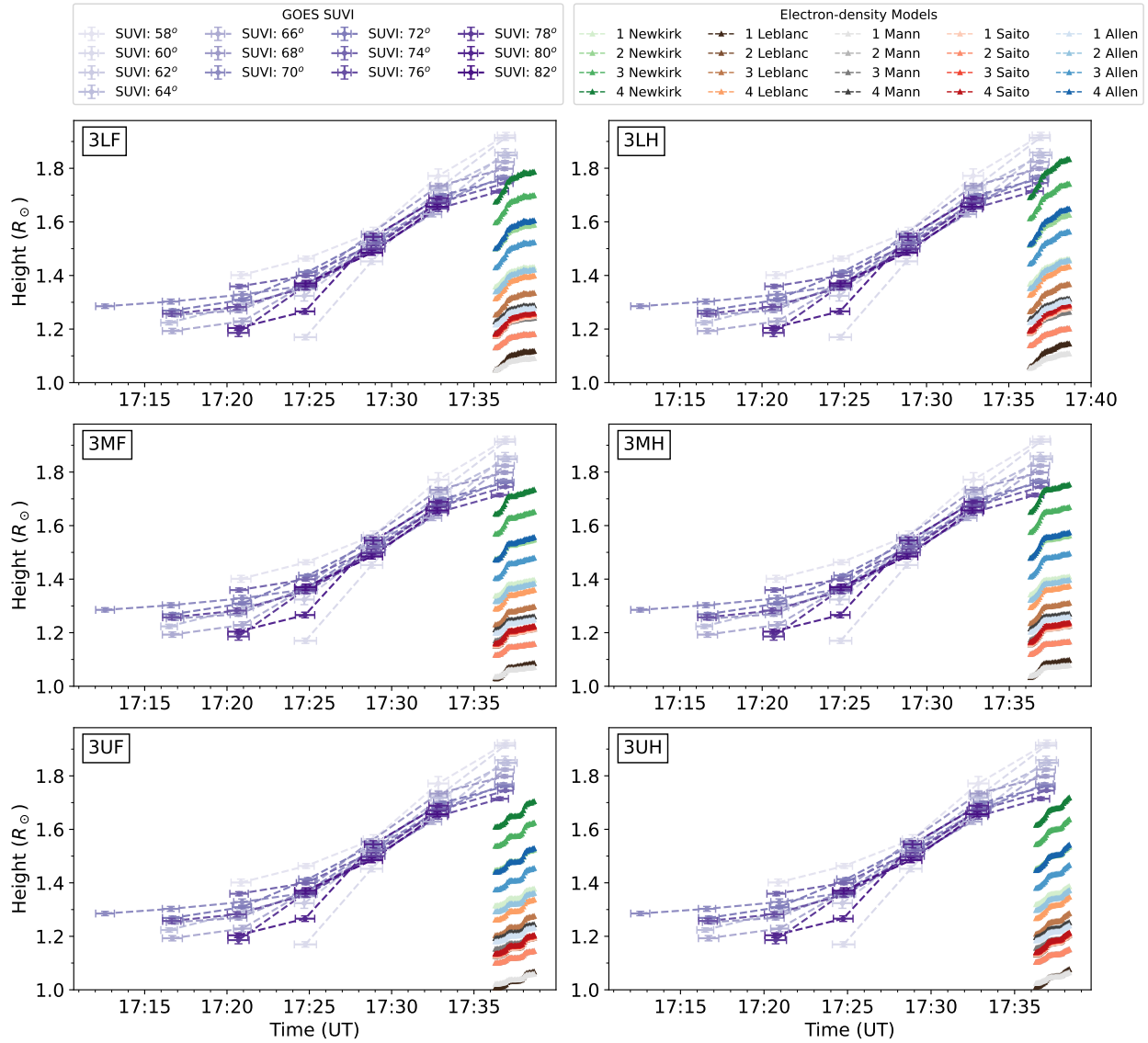
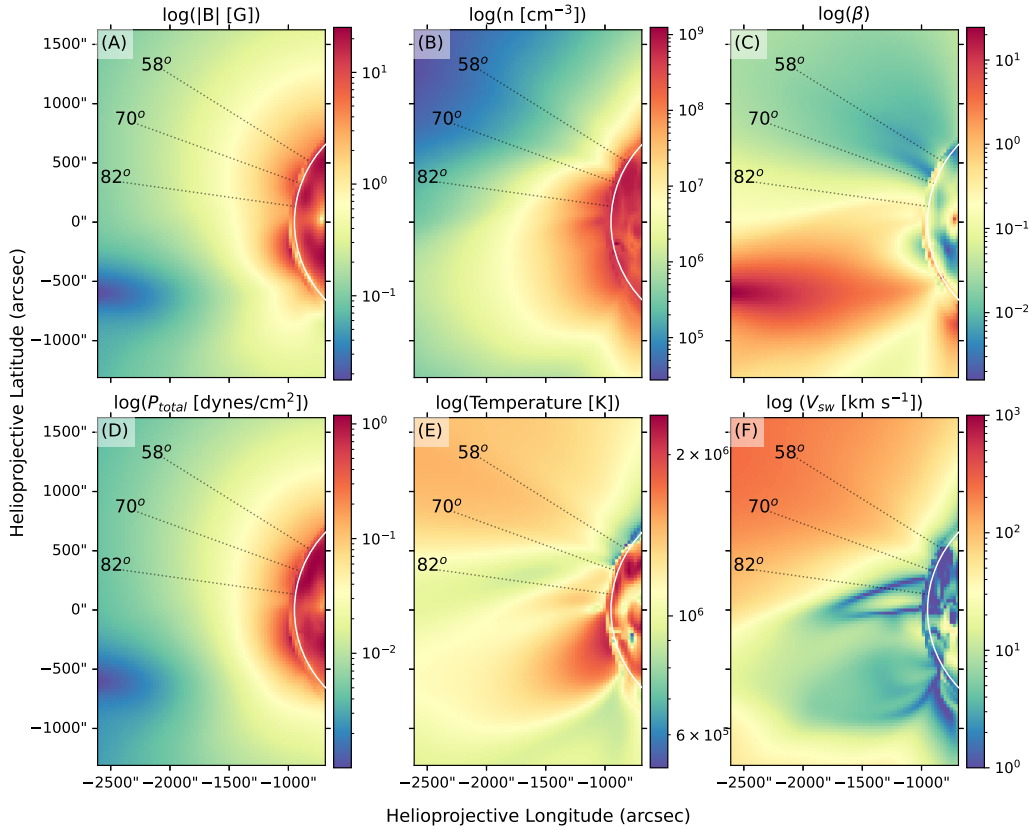
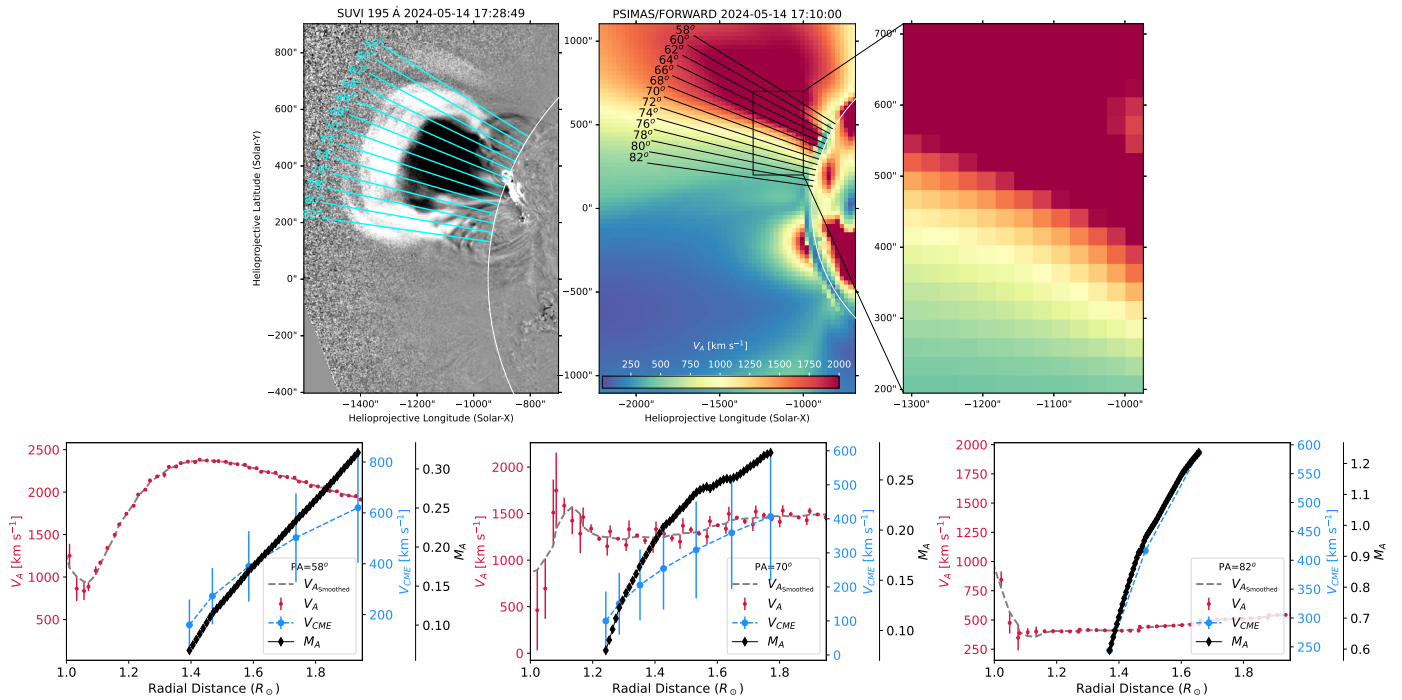


Fig. A.4. Third type II burst.



**Fig. A.5.** Set of FORWARD maps for the coronal parameters. The dotted black lines are the radial slits at the flanks and centre of the CME. Top to bottom: Total magnetic field strength (A), density (B), plasma- $\beta$  (C), total pressure (D), temperature (E), and solar wind speed (F). The colour scale is shown in the log-scale to increase the contrast of details.



**Fig. A.6.** Top panel: SUVI running-ratio image and the pre-eruption Alfvén speed map from the PSI-MAS FORWARD model, with the radial slits. The zoomed-in view at the centre of the eruption location shows the differences between the north and south of the AR clearly, as well as the pixelation. The Alfvén speed profiles are jagged due to the pixelation. Bottom panel: Temporal evolution for the CME speed, the Alfvén speed, and the Mach number for the upper, middle, and lower slits. The Mach number is estimated by dividing the CME speed by the Alfvén speed after they are interpolated to match their lengths.